

## The Impact of Desertification in the Mongolian and the Inner Mongolian Grassland on the Regional Climate

YONGKANG XUE

*Center for Ocean–Land–Atmosphere Studies, Calverton, Maryland*

(Manuscript received 16 May 1995, in final form 7 March 1996)

### ABSTRACT

This is an investigation of the impact of and mechanisms for biosphere feedback in the northeast Asian grassland on the regional climate. Desertification in the Inner Mongolian grassland has dramatically increased during the past 40 years. The Center for Ocean–Land–Atmosphere Studies atmospheric general circulation model, which includes a biosphere model, was used to test the impact of this desertification. In the grassland experiment, areas of Mongolia and Inner Mongolia were specified as grassland. In the desertification experiment, these areas were specified as desert. Each experiment consists of six integrations with different atmospheric initial conditions and different specifications of the extent of the desertification area. All integrations were 90 days in length, beginning in early June and continuing through August, coincident with the period of the East Asian summer monsoon.

The desertification had a significant impact on the simulated climate. During the past 40 years, the observed rainfall has decreased in northern and southern China but increased in central China, and the Inner Mongolian grassland and northern China have become warmer. The simulated rainfall and surface temperature differences between the desertification integrations and the grassland integrations are consistent with these observed changes.

The water balance and surface energy balance were altered by the desertification. The reduction in evaporation in the desertification experiment dominated the changes in the local surface energy budget. The reduction in convective latent heating above the surface layer enhanced sinking motion (or weakened rising motion) over the desertification area and over the adjacent area to the south. Coincidentally, the monsoon circulation was weakened and the rainfall was reduced.

### 1. Introduction

There is an increasing concern that anthropogenic changes in land cover, such as desertification and deforestation, may affect climate by changing the hydrological cycle and surface energy balance. During the last decade, the desire to have a better understanding of the regional and global impact of land surface changes has stimulated studies of land surface–atmosphere interactions using coupled atmosphere–biosphere models. Among these studies, the impact of Amazonian deforestation and Sahel desertification have been widely investigated because both areas have undergone large-scale land surface degradation and the Sahel has suffered a long-term drought (e.g., Charney 1975; Dickinson and Henderson-Sellers 1988; Xue et al. 1990; Nobre et al. 1991; Xue and Shukla 1993; Xue et al. 1996a). Xue and Shukla (1993, 1994) showed that changes in land surface conditions play an important role in producing the rainfall anomaly observed in the Sahel during the 1980s. Thus far, most land sur-

face–atmosphere interaction studies have focused on the tropical region, where the impact of thermodynamic forcing from the lower boundary on the large-scale flow is large and the impact of nonlinear dynamical flow instabilities is relatively small.

Observations show that decadal-scale climate anomalies and land surface degradation have also occurred in the middle latitudes. East Asia has experienced rainfall and temperature anomalies in conjunction with the desertification of Inner Mongolia over the last 40 years, although the extent and degree of desertification and drought are not as severe as in the Sahel. In this study, the impact of the desertification of the Mongolian and Inner Mongolian grassland on the regional climate is explored. Because the summer climate in the East Asian continent is dominated by the monsoon, the impact of land surface processes on some of the East Asian monsoon features will be investigated in this study.

The Inner Mongolian grassland is located in northern China, extending from about 40° to 50°N and from about 107° to 125°E. This steppe is part of the great Euro–Asian grassland and is a transitional climate zone between the humid monsoon region and the inland arid area. To the south of this area, the vegetation is dominated by broadleaf deciduous trees and crops. Arid and

---

*Corresponding author address:* Dr. Yongkang Xue, Center for Ocean–Land–Atmosphere Studies, 4041 Powder Mill Road, Suite 302, Calverton, MD 20705-3106.

semiarid regions lie to the north and west. This transition zone is sensitive to natural variations and anthropogenic changes. Historical records reveal that significant southward and northward movements of the belt of mixed pasture and agricultural land use have taken place during the last 2000 years, coincident with climate changes. This belt is located at the southern boundary of the transitional zone and corresponds to the area having a 20% frequency of occurrence of at least 400 mm of precipitation annually (Ye 1992; Ye and Chen 1992). Movement of the mixed land-use belt is indicative of changes in both temperature and precipitation.

Part of the mixed land use belt has shifted southeastward significantly over the past 40 years, reflecting a trend of increasing aridity during this time (Fu 1992). Observations in mainland China from 1951 to 1990 reveal that, in general, China has been drying since the 1950s. For example, the rainfall in Beijing decreased from 820 mm/yr in the 1950s to 550 mm/yr in the 1980s (Chen et al. 1992). The 1950s was a wet period for many regions of the world, including the Sahel, China, and India. This wet period was replaced by dry episodes in the early 1960s. It has been suggested that these changes are associated with natural variability (Lamb 1978; Yan et al. 1990). This dry period ended in most areas in the mid-1970s when the precipitation returned to normal. However, the drought has persisted in China but with less intensity than in the Sahel.

The summer rainfall over the East Asian continent is mainly determined by the monsoon circulation, which brings abundant moisture to the region. The moisture in the summer monsoon flow comes from three major sources: the Indian monsoon, the South China Sea monsoon, and the southeast trade wind. The monsoon rainfall starts in southern China in May and moves northward. The monsoon reaches the Yangtze River in June and northern China in July and August. The maximum rainfall belt retreats to the South China Sea in September (Chen et al. 1991).

Figure 1 (after Liang et al. 1992, Fig. 3) shows the Z scores for the June, July, and August (JJA) mean precipitation for three regions of China during the past 40 years. Region 1 is located to the north of the Yellow River and to the south of Inner Mongolia, covering the area from 34° to 41°N and from 110° to 120°E. Region 2 is along the south side of the Yangtze River, covering the area from 25° to 31°N, 108° to 121°E. Region 3 is located between region 2 and the South China Sea, covering the area from 25°N to the coast and from 110° to 121°E. These three regions are referred to as the North China region, the Yangtze River region, and the South China region, respectively, as traditionally used in Chinese documents. Their locations are marked in Fig. 2. The Z score is the standard normal deviate of precipitation and is used to describe the categories of precipitation. According to the definition of Liang et al. (1992), a Z score of 4 represents normal rainfall con-

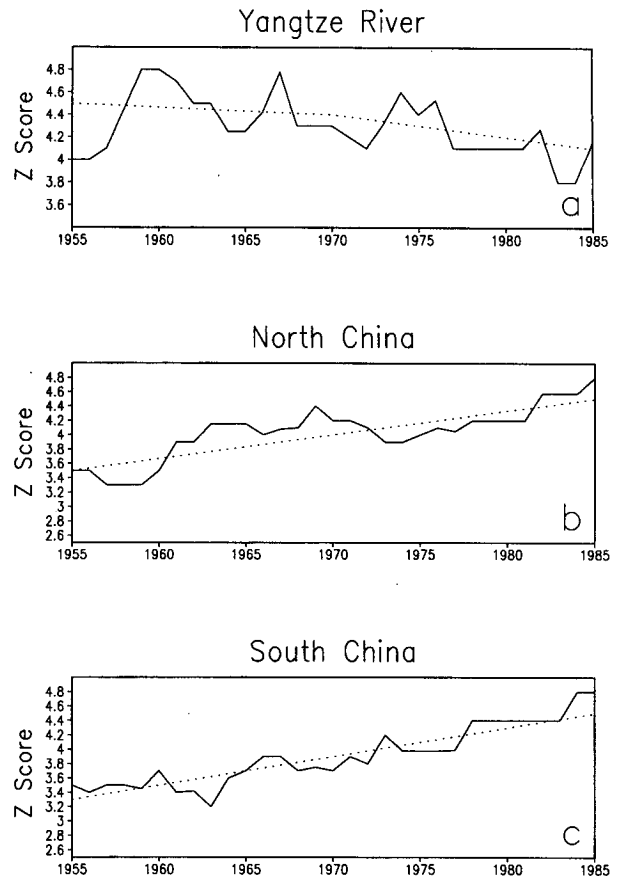


FIG. 1. JJA Z-score time series (see text) for (a) Yangtze River, (b) North China, and (c) South China. The dashed lines are from a least squares fit.

ditions, higher Z scores represent dry conditions, and lower Z scores represent wet conditions. Figure 1 shows that both the South China region and the North China region became dry during the last 40 years. Concurrently, the precipitation has increased in the Yangtze River region. Over the country as a whole, precipitation has decreased. June, July, and August are within the summer monsoon season in China; thus these changes are likely related to variations in the East Asian summer monsoon.

Although much research has been carried out to investigate the impact of climate changes on the northeast Asian climate transition zone, the impact of biosphere feedback in this area has not been studied. I conducted sensitivity experiments to investigate the impact of and mechanisms for land surface degradation on the summer monsoon and temperature anomalies in this region.

In northern China, there are vast areas of desertification-prone land (about 334 000 km<sup>2</sup>), of which about 176 000 km<sup>2</sup> is already desertified (Zhu et al. 1988). The desertified area has expanded at a rate of 1560 km<sup>2</sup> per year from the 1950s to the 1970s. The desertification there can be classified into three types: desertifi-

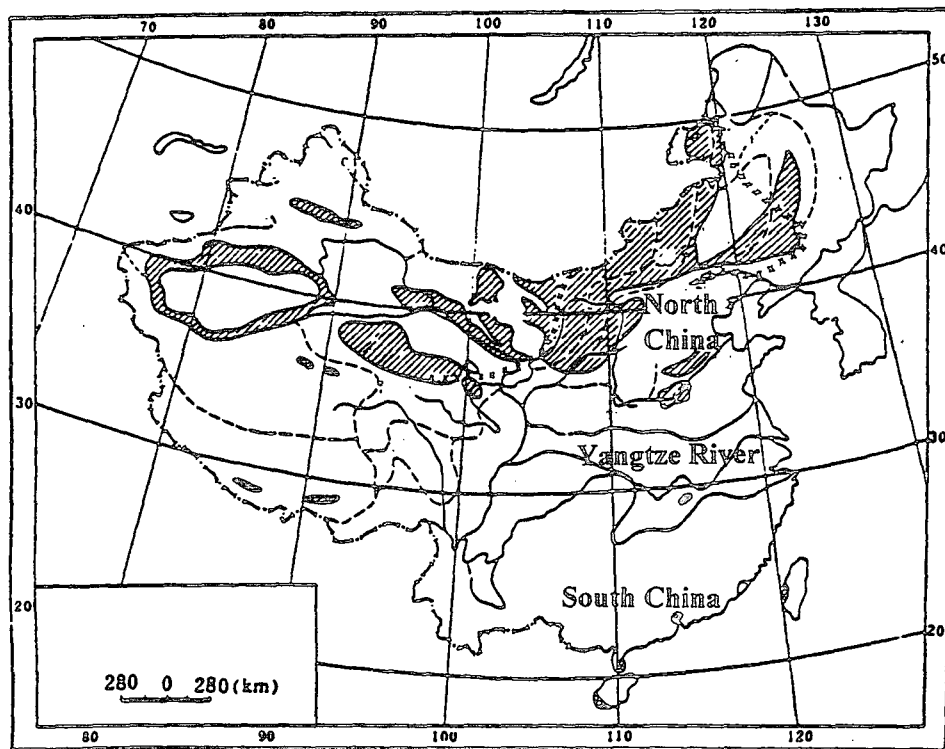


FIG. 2. China desertification map (shaded area) (after Dong 1989).

cation of sandy steppe, the reactivation of fixed dunes, and the encroachment of sand dunes. Figure 2 shows the desertified area of China, a large part of which is located in the Inner Mongolian grassland (Dong 1989). This desertification map is based on the China desertification map of Zhu et al. (1988), which provides more detailed structure. There are a number of definitions of desertification that involve many geological, economical, ecological, and biological concepts, which can be found in Zhu et al. (1988) and Xue and Shukla (1993). I will not discuss these in detail in this paper. The desertification areas closely follow the region of mixed

pasture and agricultural land use, where the ecosystem is especially vulnerable to external (natural and anthropogenic) forcing. The Inner Mongolian grassland is the main pasture region in China. The rapidly expanding population, increasing human land use, and agricultural development have led to environmental degradation. Overcultivation on the steppe, overgrazing, and full wood cutting are responsible for 25%, 28%, and 32% of the total area of desertification from the 1950s through the 1980s, respectively (Zhu et al. 1988). Thus, increasing human activities have accelerated the development of desertification in the 1980s.

TABLE 1. The development of desertification in Inner Mongolia (Zhu and Tao 1993). All regions are located between 35° and 45°N, 105° and 120°E.

Regions	Representative region area (km <sup>2</sup> )	Desertified land area				Period
		in mid-1970s		in mid-1980s		
		(km <sup>2</sup> )	(%)	(km <sup>2</sup> )	(%)	
Chahar	9050	2848	31.5	5992	66.1	1975-87
Ulanqab	46 660	2031	4.4	4055	8.7	1975-87
South Ordos	6551	5729	87.5	5248	80.1	1977-86
Mid-Korquin	2709	1270	46.9	1152	42.5	1974-88
Mid-Alxa	1573	1171	74.5	1308	83.2	1974-84
West Alqa	16 200	3480	21.5	5955	36.8	1975-86
North Hebei	17 250	2524	14.6	4608	26.7	1975-87

Table 1 shows the development of desertification in some regions of Inner Mongolia from the middle 1970s through the middle 1980s. Although the desertification extent was slightly reduced in two small regions, the amount of desertified land has increased significantly. Several large regions (listed in Table 1) have almost doubled their desertification area during these ten years. At this rate of desertification, the current 176 000 km<sup>2</sup> of desertified land will increase to 251 000 km<sup>2</sup> by the year 2000 (Zhu et al. 1988).

The area near the boundary between Inner Mongolia and Mongolia is also characterized as a moderate desertification region (Dregne and Chou 1992). However, due to the limited availability of data from Mongolia, the observations described here focus on the Chinese side. In the numerical experiments, the land surface characteristics are changed in both regions because of their close geographical proximity.

The model is described in section 2. The experimental design is described in section 3. The results from control integrations and the impact of desertification on the surface energy balance, surface temperature, rainfall, the surface water budget, and the atmospheric circulation are discussed in section 4. A summary is presented in section 5.

## 2. Model description

The Center for Ocean–Land–Atmosphere Studies (COLA) atmospheric general circulation model (GCM) is a modified version of the National Meteorological Center (NMC) global spectral model with rhomboidal truncation at wavenumber 40 (Sela 1980; Kinter et al. 1988; Fennessy et al. 1994). The prognostic computations are done in the spectral domain and the physical processes are computed on a grid (approximately 1.8° lat × 2.8° long). The model is discretized into 18 vertical layers. The parameterizations for physical processes include:

- 1) an efficient radiation scheme that resolves the diurnal cycle and includes terrestrial radiative heating (Harshvardhan et al. 1987) and solar radiative heating [Lacis and Hansen (1974); modified by Davies (1982)]. An interactive cloud scheme similar to the one developed by Slingo (1987) was incorporated into the GCM for the radiation calculations (Hou 1990).
- 2) the level 2.0 second-order turbulence closure scheme of Mellor and Yamada (1982) for subgrid-scale exchanges of heat, momentum, and moisture
- 3) a modified Kuo scheme for convection (Kuo 1965; Anthes 1977), shallow convection (Tiedtke 1984), and large-scale condensation
- 4) a gravity wave drag parameterization, which follows that of Alpert et al. (1988).

The SSiB model (Xue et al. 1991), which is a simplified version of the Simple Biosphere model (SiB) of Sellers et al. (1986), is used to model the land surface

in the COLA GCM. SSiB has three soil layers and one canopy layer and includes eight prognostic variables: soil wetness in three soil layers; temperature at the canopy, ground surface, and deep soil layers; water stored on the canopy; and snow stored on the ground.

There are 12 vegetation types in SSiB. These include tall vegetation, short vegetation, arable crops, and desert (Dorman and Sellers 1989). The main sources of data for the distribution of the world vegetation types were the physiognomic classification of Kuchler (1983) and the land use database of Matthews (1984, 1985). A parameter set for each of the 12 SiB and SSiB types was created based on a variety of sources (Dorman and Sellers 1989; Willmott and Klink 1986). Many of the parameters in SSiB are invariant with season. However, seasonally varying monthly values of leaf area index and green leaf fraction are prescribed. The prescription of the crop vegetation type is different from that of other vegetation types: the vegetation cover, leaf area index, greenleaf fraction, leaf orientation, and root length are varied according to the growing season, which is a function of latitude and time.

In the COLA GCM, the SSiB parameters are assigned to each grid square based on the input vegetation map and month. These parameters and the solar zenith angle and snow cover determine the surface albedo and the surface radiation budget. The surface model provides the GCM with the land–atmosphere fluxes of latent heat, sensible heat, momentum, and radiation. A detailed model description can be found in Xue et al. (1991, 1996a,c).

## 3. Experimental design

This study is designed to investigate the effects of biosphere feedback in the Mongolian and Inner Mongolian grassland on the regional climate. The climate in this region is temperate and semiarid with continental characteristics. The predominant vegetation types are those found on temperate steppes. Meadow steppe, typical steppe, and dry steppe types occur from the southeast to northwest, respectively (Zhu et al. 1988). The desertification process in this area is manifested by a reduction of the vegetation cover as well as by changes in the vegetation composition.

Observations in the Horqin Steppe, located in northeast Inner Mongolia, revealed that in the area undergoing desertification the vegetation cover has decreased from 70%–80% to 30%–40%. The dominant species in the Horqin Steppe are shrubs, perennial herbs, and *Artemisia*. In desertified areas, the plants are dwarfed and the foliage is reduced. The average height of the desertified herb is 40–50 cm and the fresh biomass is 3000 kg ha<sup>-1</sup>, whereas the normal height and biomass are more than 60 cm and more than 4500 kg ha<sup>-1</sup>. In the severe desertification area, the plant species are similar to those in the ongoing desertification area, but the vegetation is only 20%–25% of its

TABLE 2. Vegetation parameters for types 7 and 11.

Type	Mean surface albedo	Roughness length (m)	Soil hydraulic conductivity at saturation (m s <sup>-1</sup> )	Soil moisture potential at saturation (m)	Total soil depth (m)	Vegetation cover	Mean leaf area index
7	0.23	0.07	0.2E-4	-0.086	1.49	0.9	3.0
11	0.32	0.01	0.176E-3	-0.035	0.49	0	0

normal height, or even 10% in the most severe desertification area. The fresh biomass in desertification regions is reduced to 1500 kg ha<sup>-1</sup>. In severe desertification regions, it is reduced to 375–750 kg ha<sup>-1</sup> (Zhu et al. 1988).

In this sensitivity study, I assign two SSiB vegetation types in the COLA GCM to parts of Mongolia and Inner Mongolia: grass (type 7 in SSiB) for the grassland experiments and bare soil (type 11 in SSiB) for the desertification experiments. Compared with the preceding summary of the observations, it is clear that using bare soil to represent the desertification area is an exaggeration. There is a historical reason to use the bare soil vegetation type in this study. In the current COLA GCM, Kuchler's vegetation map (Kuchler 1983) is used to prescribe the vegetation classification

over Asia. This map very much exaggerates the extent of the desert area in northeast Asia. Thus, the desert area is kept as it appears in Kuchler's map in the desertification experiments, and some of the desert areas have been replaced by grassland in the grassland experiments. This is a sensitivity study, and a stronger than realistic impact may be obtained by this exaggeration of the desertification conditions. The major parameters for types 7 and 11 in SSiB are listed in Table 2. The bare soil vegetation type has no vegetation, sandy soil, low water storage, and high surface albedo.

Figure 3 shows the vegetation map currently used in the COLA GCM. Types 2, 3, 4, and 12 in this figure are broadleaf-deciduous trees, broadleaf and needleleaf trees, needleleaf-evergreen trees, and crops, respectively. This map was used for the desertification ex-

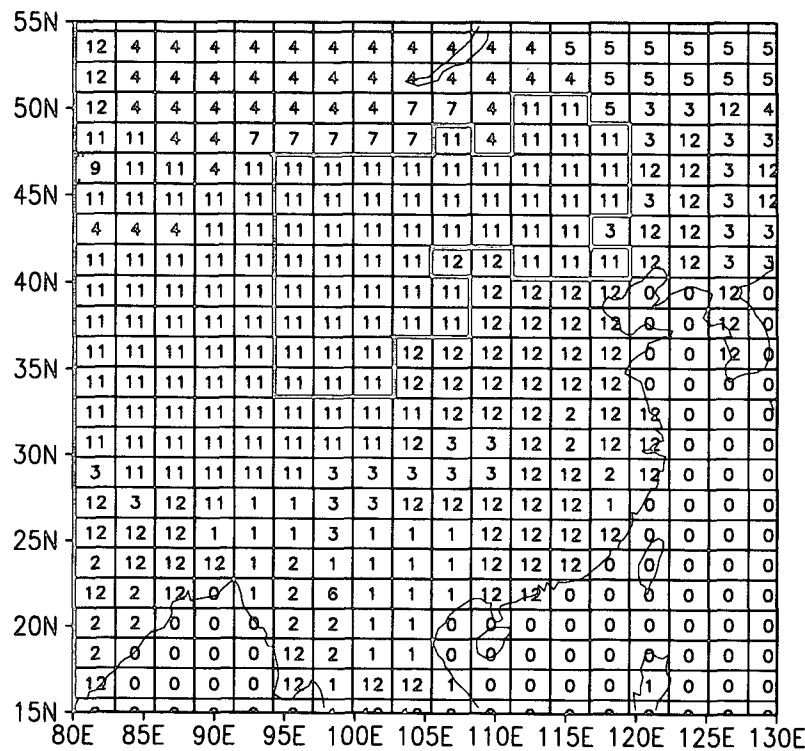


FIG. 3. Vegetation types for experiment D1. Type 1: tropical forest, Type 2: broadleaf-deciduous trees, Type 3: broadleaf and needleleaf trees, Type 4: needleleaf evergreen trees, Type 5: needleleaf deciduous trees, Type 7: grassland, Type 9: shrubs with bare soil, Type 11: bare soil, and Type 12: crops. The test area is enclosed by a thick line.

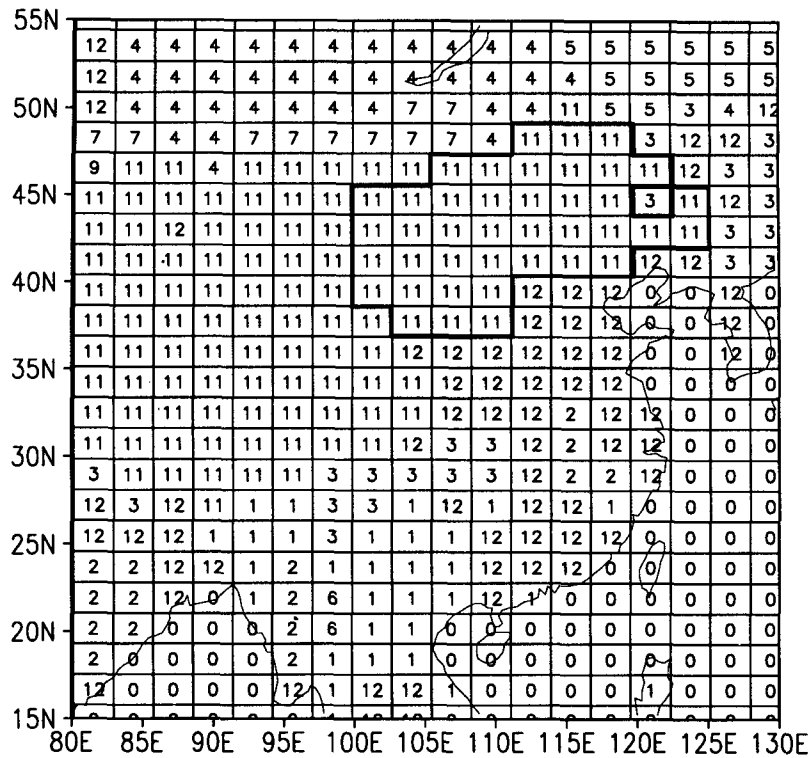


FIG. 4. Vegetation types for experiment D21.

periment. The area in Fig. 3 enclosed by a thick line was replaced by vegetation type 7 in the grassland experiment. I will refer to this area as the test area. Seasonally varying climatological sea surface temperature (SST) was used as a boundary condition for all the integrations described here. It is updated daily in the GCM. Studies have been conducted to investigate the connection between the East Asian monsoon and SST anomalies (Meehl 1987; Yanai and Li 1994; Shen and Lau 1995). Here, I focus on the impact and mechanisms of desertification-atmosphere interactions.

The desertification area in the experiment described above (Fig. 3) was larger than that observed (Fig. 2). The results from this experiment, which will be presented in the next section, show that the impact of this desertification on the rainfall anomalies was also larger than the observed change over the last 40 years.

To more realistically assess the impact of desertification, a second set of integrations was done in which the desertification area in Inner Mongolia was closer to that observed. The three integrations in this second experiment had slightly different desertification and/or grassland boundaries, but the atmospheric initial conditions were kept the same. One vegetation map in this experiment is shown in Fig. 4, in which the desertification area (i.e., the test area) is enclosed by a thick line. In this area type 11 was replaced by type 7 in the grassland experiment. The other two pairs of vegetation maps can be found in Xue (1995). This design was motivated by two considerations: 1) Due to the spatial and temporal variations of desertification, and the limitation of current technology, it is almost impossible to determine the exact extent of the observed desertification. In reality, the desertification area boundary varies

TABLE 3a. Initial conditions and boundary conditions for experiments D1 and G1. LD refers to the large desertification area. LG refers to the larger grass land.

Cases	D1			G1		
	D11	D12	D13	G11	G12	G13
Land surface condition in the test area (°)	LD	LD	LD	LG	LG	LG
Initial conditions	1 Jun 87	2 Jun 87	1 Jun 86	1 Jun 87	2 Jun 87	1 Jun 86



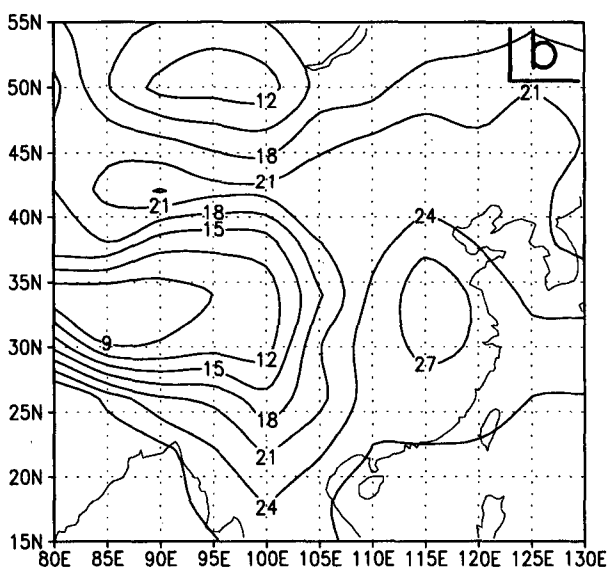
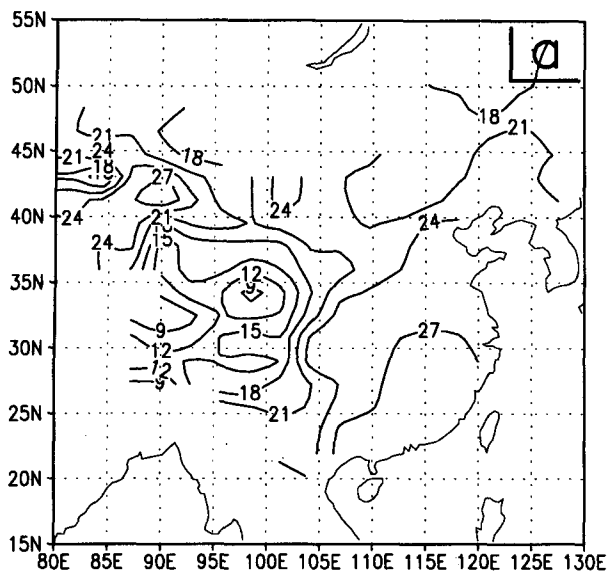


FIG. 5. JJA surface temperature from (a) observations and (b) ensemble D1. Isotherms are 9, 12, 15, 18, 21, 24, and 27 K.

simulated rainfall over this region was less than observed. This deficiency is partially related to problems with the crop model (Xue et al. 1996b). A recent study has revealed that the convection scheme also has a big impact on the rainfall simulation on this region (Fennesy 1995, personal communication).

The position of the observed summer East Asian monsoon rainfall belt is located south of the westerly jet and is highly correlated to the subtropical high and

the westerly jet (Zhu et al. 1979). Figure 7b shows the JJA zonal wind averaged from 105° to 120°E for ensemble D1. The magnitude of the westerly jet is very close to that from the European Centre for Medium-Range Weather Forecasts (ECMWF) analyses (Fig. 7a); however, the position is about 5° too far north, which is consistent with the northward shift of the simulated rainfall. The ECMWF analysis figures shown in this paper are JJA means for 1980 through 1992.

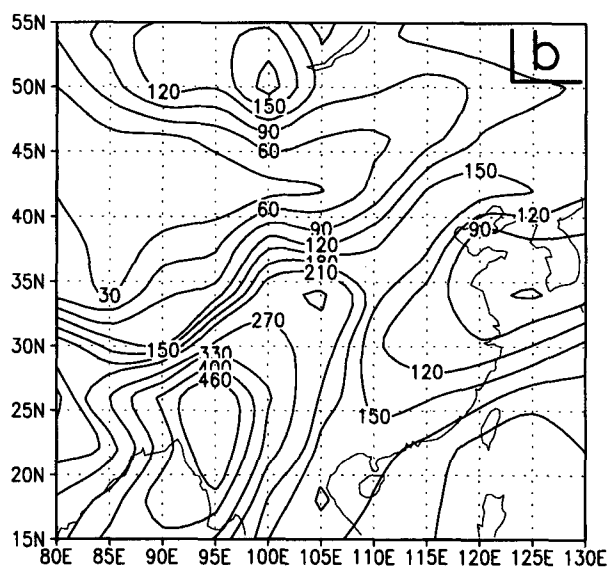
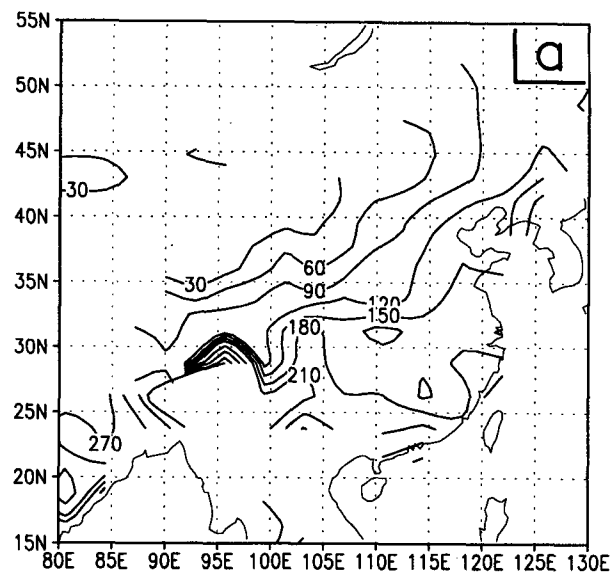


FIG. 6. JJA precipitation from (a) observations and (b) ensemble D1. Isohyets are 30, 60, 90, 120, 150, 180, 210, 270, 330, 400, and 460 mm/mo.

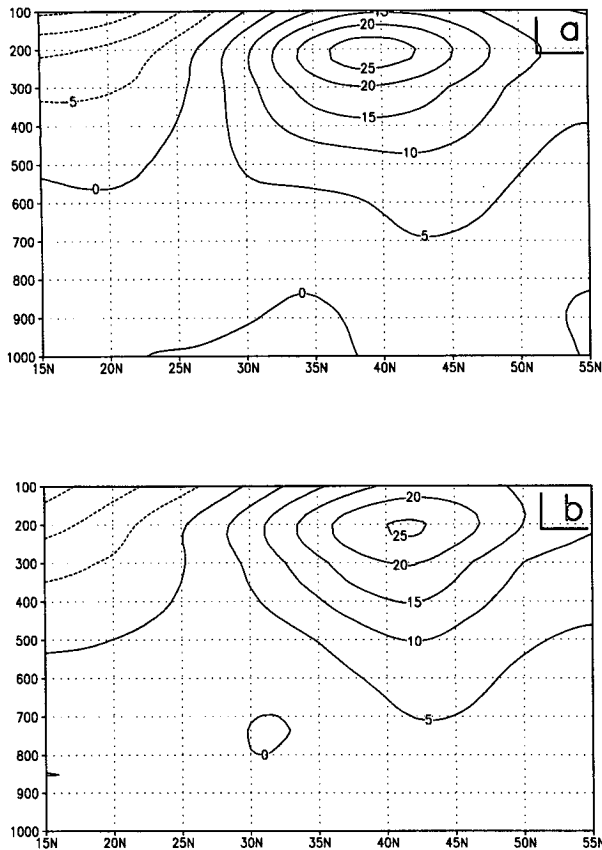


FIG. 7. JJA zonal-mean zonal wind averaged from 105° to 120°E for (a) ECMWF analysis and (b) ensemble D1. Units are meters per second.

The JJA mean wind vectors at 700 mb shown in Figs. 8a and 8b are from the ECMWF analyses and the D1 ensemble. The results at 850 mb are similar to those at 700 mb (not shown). The large-scale, low-level moist airflows from the Bay of Bengal and the South China Sea are two of the major moisture sources for the monsoon rainfall over the East Asian continent. These two airflows are well simulated. But the simulated northward airflow over the East Asian continent was stronger than observed, particularly along the eastern boundary of the Tibetan Plateau. This results in too much moisture convergence and precipitation in this area.

By and large, the COLA GCM has simulated the major patterns of the surface temperature, rainfall, and circulation over the eastern Asian continent, but with positive biases for precipitation and temperature.

*b. Impact on the surface energy balance and temperature*

The simulated surface evaporation is substantially reduced in the desertification experiments. D1 minus

G1 and D2 minus G2 JJA mean differences are shown in Fig. 9. This reduction is similar to that found in Amazon deforestation experiments (Dickinson and Henderson-Sellers 1988; Nobre et al. 1991; Xue et al. 1996a), Sahel desertification experiments (Xue and Shukla 1993), and a U.S. summer weather prediction study (Xue et al. 1996b), in which increased surface

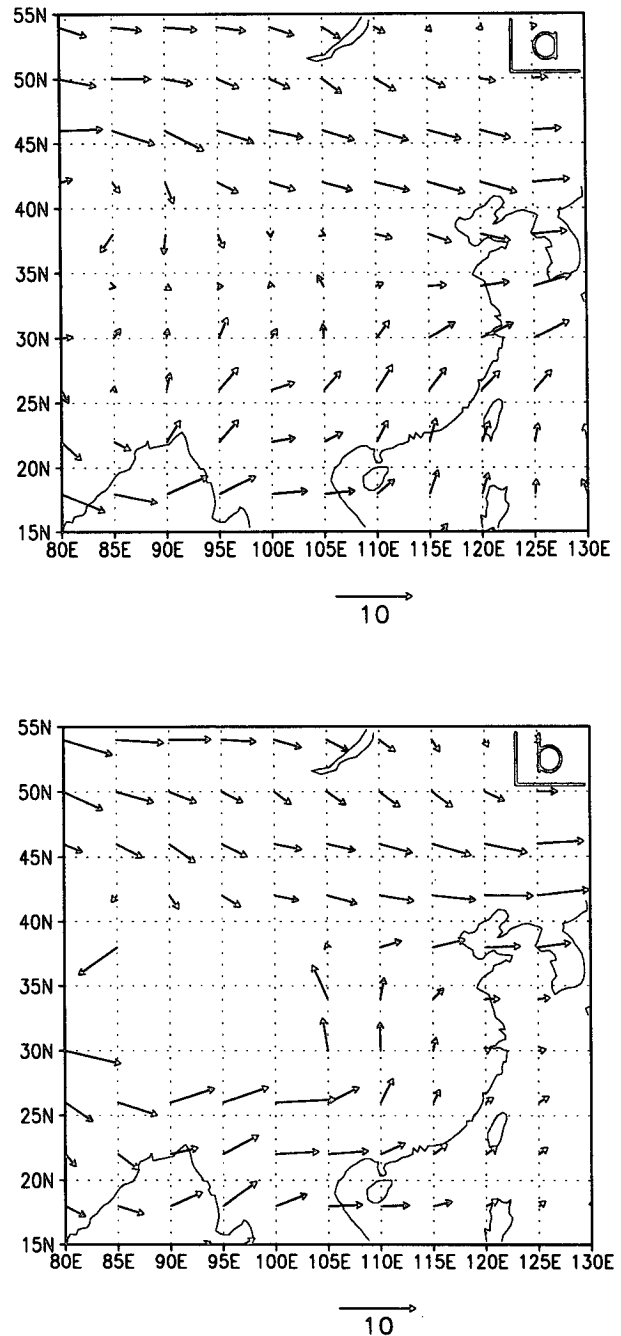


FIG. 8. JJA wind vectors at 700 mb from (a) ECMWF analysis and (b) ensemble D1. Units are meters per second.

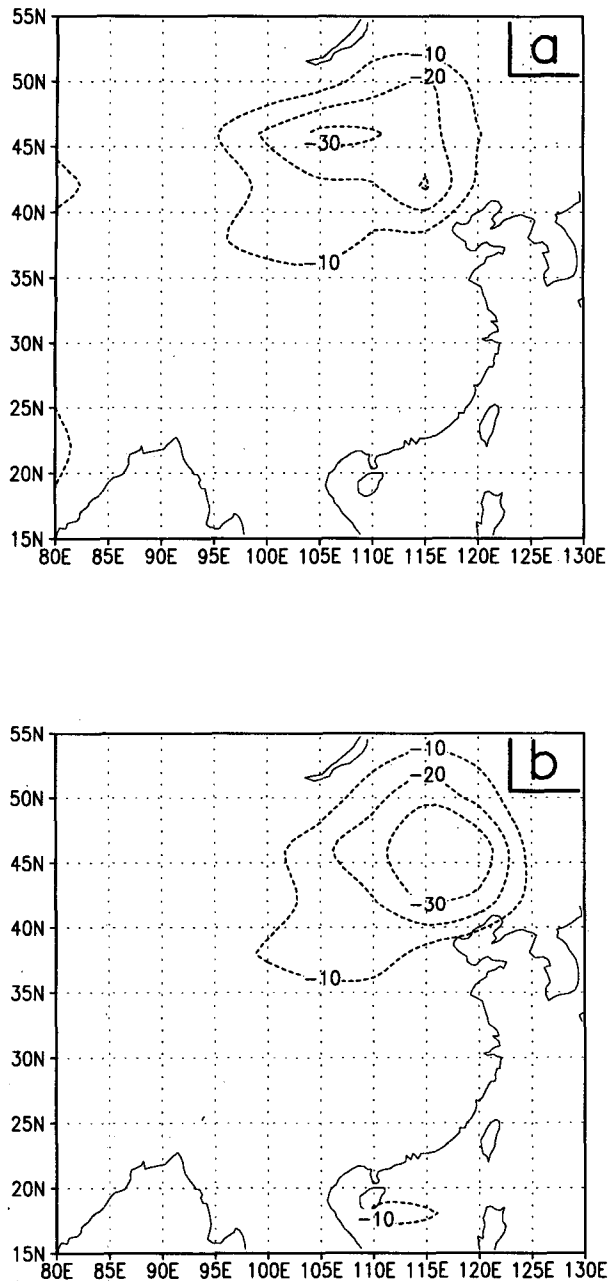


FIG. 9. JJA mean difference in latent heat flux for (a) ensemble D1 minus ensemble G1 and (b) ensemble D2 minus ensemble G2. Iso-lines are  $\pm 10$ , 20, and  $30 \text{ W m}^{-2}$ . Dashed isolines are negative.

albedo, reduced vegetation coverage, reduced soil water content, and reduced surface roughness resulted in reduced evaporation. The evaporation reduction in this study mainly occurred within the test area (Fig. 9). The reduction of the latent heat flux in ensemble D1 averaged from  $40^\circ$  to  $48^\circ\text{N}$ ,  $95^\circ$  to  $120^\circ\text{E}$  was  $21 \text{ W m}^{-2}$  (about  $0.7 \text{ mm/day}$ ). I refer to this region as the reference area for ensembles D1 and G1, for which area-averaged values are given in columns 2 and 3 of Table

4. In ensemble D2, the latent heat flux averaged over the region from  $40^\circ$  to  $48^\circ\text{N}$ ,  $100^\circ$  to  $120^\circ\text{E}$ , which I refer to as the reference area for ensembles D2 and G2, was reduced by  $23 \text{ W m}^{-2}$  (Table 4, columns 4 and 5). This reference area covers most of the test area. The latent heat fluxes from the bare soil over the reference area were actually increased by  $7 \text{ W m}^{-2}$  and  $12 \text{ W m}^{-2}$  in ensembles D1 and D2, respectively, because of the increase in bare soil fraction at each grid point. However, the evaporation increases were not proportional to the increase in bare soil area. For example, the bare soil area in ensemble D2 was nine times more than in ensemble G2, while the evaporation from the bare soil increased by about 38%, which was not enough to offset the total reduction in evapotranspiration by other factors. There was no interception loss or transpiration in the desertified area. The differences in interception loss between ensemble G1 and D1, and G2 and D2 were  $12$  and  $13 \text{ W m}^{-2}$ , respectively. The interception loss accounted for about 18% and 19% of the total evaporation in G1 and G2, respectively.

The higher surface albedo in the desertification experiments reduced the absorbed shortwave radiation over the test area despite the increased downward shortwave radiation at the surface due to the reduced cloudiness. The mean surface albedo in ensembles D1 and D2 was 0.32, which was 0.09 greater than that in ensembles G1 and G2. The shortwave radiation absorbed by the ground was reduced by about  $13 \text{ W m}^{-2}$  for ensembles D1 and D2 (Table 4) and were also limited to the test area (not shown). The downward longwave radiation was reduced slightly because of the less cloud cover (not shown). The sensible heat flux was reduced (not shown) in the area where the shortwave radiation absorbed by the ground was reduced by a large amount. In areas where the shortwave radiation absorbed by the ground was reduced by a small amount, the sensible heat flux either did not change or increased. The net reduction in the sensible heat flux over the entire test area was not large. The energy budget changes at the surface are listed in Table 4. From Table 4, it is clear that the latent heat flux differences dominate the energy budget changes. The total amount of the reduction in the latent heat flux and the sensible heat flux in ensembles D1 and D2 was larger than the reduction in shortwave radiation. The upward longwave radiation was increased by about  $10 \text{ W m}^{-2}$ , thus balancing the energy budget. The total outgoing radiation flux at the top of the atmosphere was also increased by  $5 \text{ W m}^{-2}$  due to the higher surface temperature and less cloud cover.

The mean surface air temperature over the reference area was higher in D1 and D2 than in G1 and G2, by 0.7 and 1.3 K, respectively (Figs. 10b and 10c). The temperature increase in the atmosphere occurred only at low atmospheric levels below 850 mb (not shown). The upper atmosphere became cooler by about  $0.5^\circ\text{C}$ . Based on observations from 410 stations over China,

TABLE 4. Energy balance at the surface averaged over 95°–120°E and 40°–48°N for ensembles D1 and G1 and over 100°–120°E and 40°–48°N for D2 and G2. Units are watts per squared meter for fluxes and degrees Celsius for temperature.

	Ensemble G1	D1 – G1	Ensemble G2	D2 – G2
Absorbed shortwave radiation	243	–13	237	–14
Downward longwave radiation	330	–9	331	–4
Upward longwave radiation	429	7	426	11
Cloud cover	0.41	–0.04	0.43	–0.04
Latent heat flux	64	–21	70	–23
Interception loss	15	–12	15	–13
Latent heat flux from bare soil	30	7	31	12
Sensible heat flux	80	–8	72	–6
Surface air temperature	20.7	0.7	20.4	1.3

Chen et al. (1994) found that the yearly mean surface air temperature increased over most of China during the past 40 years, mainly during winter. The surface temperature over northwestern China and Inner Mongolia had the largest increase. In summer, much of China became cooler. However, over the Inner Mongolian grassland the summer surface air temperature was warmer during the 1980s. Figure 10a shows the JJA surface air temperature difference between the 1980s and the 1950s based on data from the 336 stations described in section 3. This figure is similar to Fig. 9 in Chen et al. (1994), which is based on 410 stations. The warm area in northern China in Fig. 10a is consistent with the desertification area over the Inner Mongolian grassland (Fig. 2) and with the D2 minus G2 surface air temperature differences (Fig. 10c). The temperature in D1 relative to G1 is also increased (Fig. 10b). But the D1 – G1 temperature anomaly region is much larger than that observed due to the generous prescription of the desertification area.

### c. Impact on rainfall and the surface water budget

As noted in the introduction, precipitation in China has generally decreased during the past forty years, particularly in southern China and northern China. There is a “sandwich” pattern: negative changes to the south and north of the Yangtze River and a positive change in between. Droughts in northern China mainly occur during July and August. Figure 11a shows the observed JJA rainfall difference between the 1980s and the 1950s.

Figures 11b and 11c show the rainfall differences between ensembles D1 and G1, and D2 and G2, respectively. The simulated rainfall was reduced in the desertification area and the surrounding areas but increased to the south. The negative rainfall anomaly in northern China was large in magnitude and extended westward compared to that observed. The simulated positive anomaly was located to the southwest of the observed positive anomaly. The negative rainfall anomaly observed in southern China was not simulated. Another negative anomaly was simulated to the southwest of the simulated positive anomaly

area. Compared with observations, the simulated axis of the negative–positive–negative pattern was tilted to the southwest and basically follows the monsoon airflow from the Bay of Bengal. The East Asian monsoon has several moisture sources, as mentioned earlier. In simulations with the COLA GCM, the airflow from the Bay of Bengal dominates the East Asian monsoon and was greatly affected by the desertification.

In both D1 and D2, the rainfall reductions occurred within the desertification area but also to the south of the desertification area. The rainfall was reduced by more than 10% in the desertification experiments. The simulated negative rainfall anomaly area generally included the observed mixed land use belt. Table 5 shows the rainfall anomaly for D1 and D2 averaged over the area with the maximum rainfall reduction (34°–48°N, 100°–115°E). The rainfall anomalies in both experiments started to develop in the desertification area in the first month and became much stronger during July and August. In the historical record, the mixed land use belt has been sensitive to the global-scale climate changes. Its southward or northward movements were closely related to global temperature variations (Ye 1992). The results from this study suggest that the climate in this area may also be sensitive to land surface conditions.

Figure 12 shows the D2 minus G2 differences of soil moisture in the rooting zone. The D1 minus G1 differences are similar (not shown). The soil moisture reduction was limited to the test area. Outside this area, the soil moisture changes were not very large and the soil water content was close to the field capacity. About 60% of the rainfall changes there directly became runoff. Studies have shown that land surface models go through a long spinup process in simulating the soil moisture (e.g., Yang et al. 1995). This spinup process affects the simulated ground water partitioning between the soil water content, surface runoff, and drainage. For a comprehensive and quantitative investigation of the ground water budget, a longer-term integration is required. The current study does not address such spinup processes.

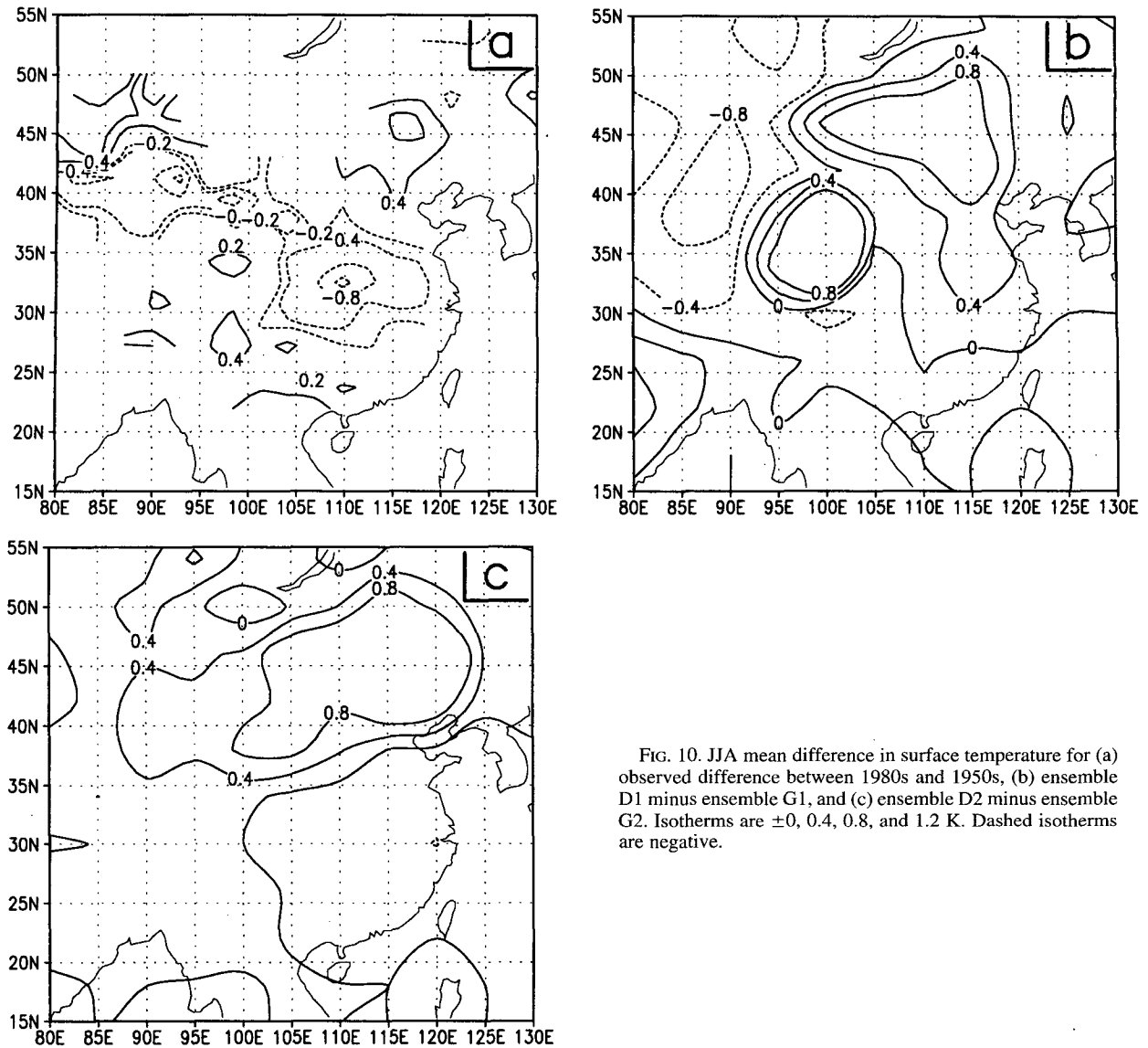


FIG. 10. JJA mean difference in surface temperature for (a) observed difference between 1980s and 1950s, (b) ensemble D1 minus ensemble G1, and (c) ensemble D2 minus ensemble G2. Isotherms are  $\pm 0, 0.4, 0.8,$  and  $1.2$  K. Dashed isotherms are negative.

#### d. Impact on circulation

Within the test area, the reduction in rainfall was less than the decrease in surface evaporation in both ensembles D1 and D2. Outside the test area, no substantial evaporation difference was found. The large-scale circulation and moisture flux convergence must be examined to understand the rainfall differences.

The main airflows that bring moisture to the East Asian continent in summer are the Indian monsoon and South China Sea summer monsoon. Any substantial change in these airflows would have a significant impact on the East Asian monsoon. Since the results from ensembles D1 and D2 are very similar, I present only results from ensemble D2 in this section. The deserti-

fication area in D2 is relatively close in extent to that observed. Figure 13 shows the three-month mean wind vector difference at 700 mb between ensembles D2 and G2. After desertification, the monsoon flow is weaker. The wind vector differences at 850 mb are very similar (not shown).

Figure 14 shows the JJA mean D2 minus G2 difference in the vertically integrated moisture flux convergence. In part of the test area, the vertically integrated moisture flux convergence slightly increased in D2 due to the higher surface temperature and increased rising motion. This increase was not large enough to compensate for the reduction in evaporation. As previously discussed, the rainfall was reduced in the test area. The differences in the vertically integrated moisture flux convergence outside the test area are very consistent

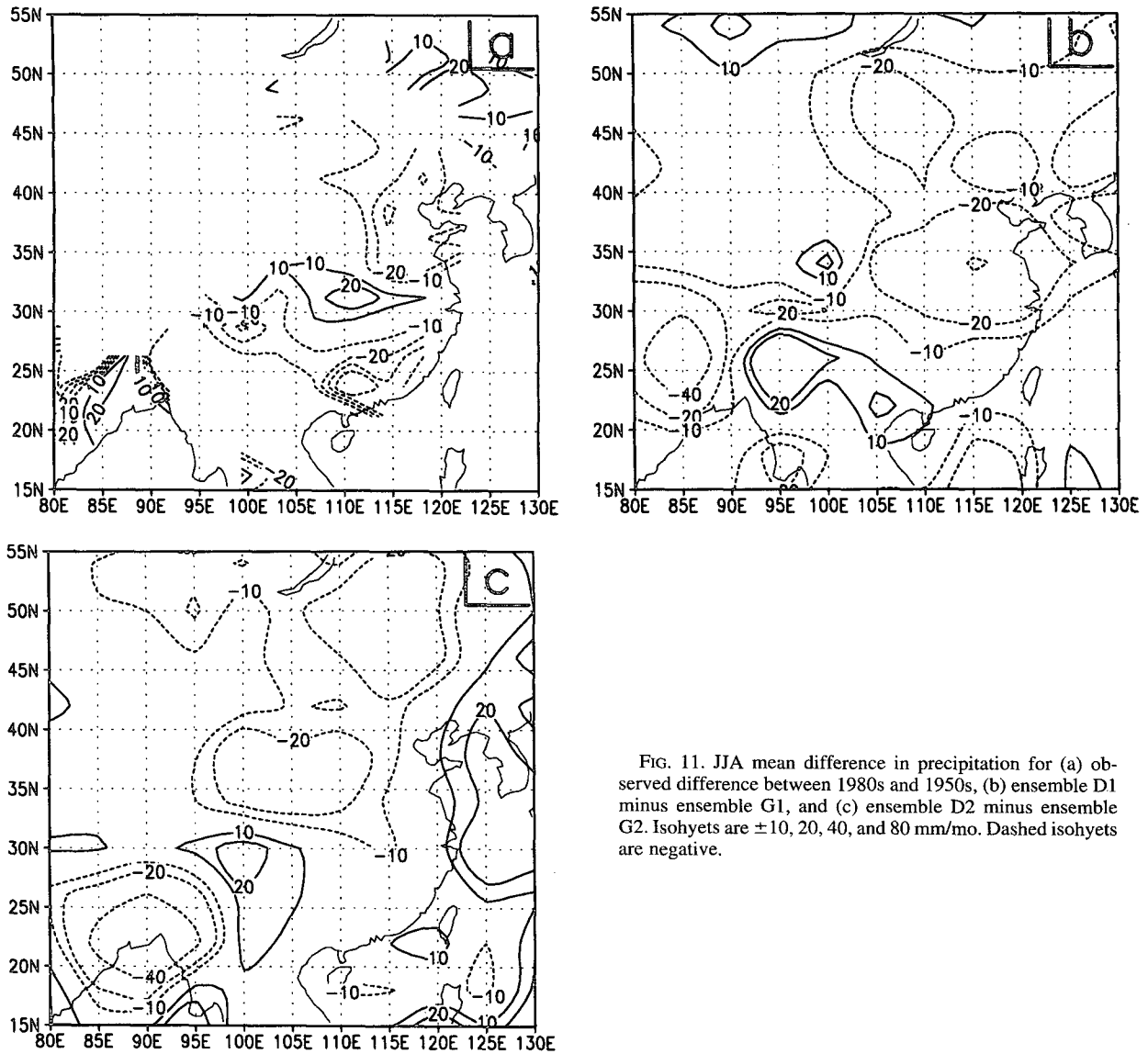


FIG. 11. JJA mean difference in precipitation for (a) observed difference between 1980s and 1950s, (b) ensemble D1 minus ensemble G1, and (c) ensemble D2 minus ensemble G2. Isohyets are  $\pm 10, 20, 40,$  and  $80$  mm/mo. Dashed isohyets are negative.

with the local rainfall variations (Fig. 11). This suggests that large-scale circulation changes are responsible for the rainfall changes outside the test area. The changes in the moisture flux convergence mainly occurred below 700 mb (not shown). An examination of the precipitable water field reveals that the atmosphere was drier in D2 north of 30°N (not shown). This reduction in moisture content occurred mainly below 700

mb. To the south of the desertification area there was an area with increased moisture flux convergence (or reduced moisture flux divergence).

Figure 15 shows the D2 minus G2 difference in the total diabatic heating at 500 mb, where the most convective condensation occurred. The anomaly pattern in this figure is consistent with that of the D2 minus G2 rainfall difference (Fig. 11c). The total diabatic heating consists of the radiative heating, diffusive heating, and convective heating, etc. Among these components, the changes in the convective heating rate account for about 90% of the total diabatic heating difference in the test area and vicinity. After the air loses heat, the air descends and compresses adiabatically to maintain thermal equilibrium. The difference in the vertical velocity ( $\omega$ ) at 500 mb (not shown) is consistent with the

TABLE 5. Simulated rainfall anomaly time series.

	Jun	Jul	Aug	JJA mean
D1 - G1 (mm/mo)	-9.5	-22.8	-18.6	-16.9
D2 - G2 (mm/mo)	-7.8	-22.2	-27.9	-19.3

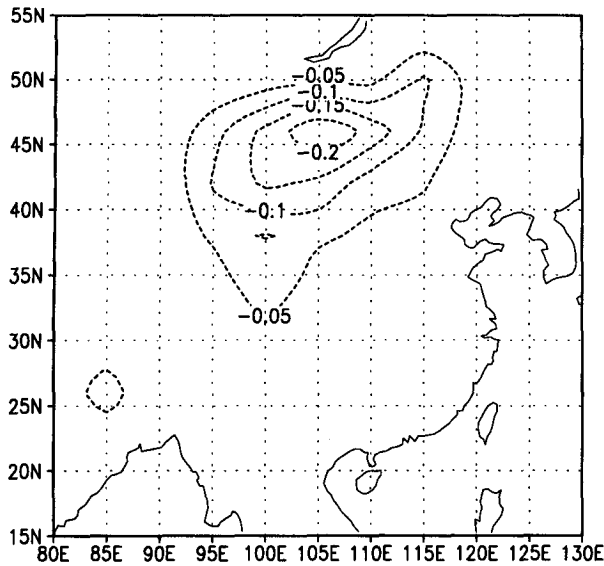


FIG. 12. JJA mean difference in soil wetness of the rooting zone for ensemble D2 minus ensemble G2. Isolines are  $\pm 0.05, 0.1, 0.15, 0.2$ . Dashed isolines are negative.

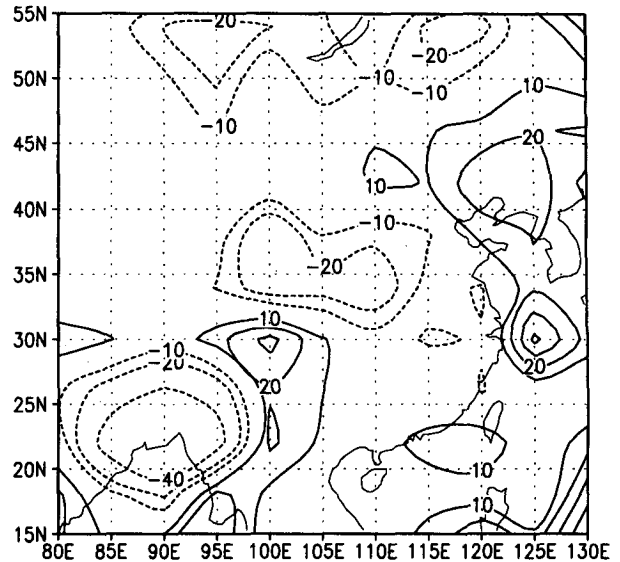


FIG. 14. JJA difference in vertically integrated moisture flux convergence for ensemble D2 minus ensemble G2. Equivalent isohyets are  $\pm 10, 20, \text{ and } 40$  mm/mo. Dashed isohyets are negative.

precipitation difference (Fig. 11c) and the total diabatic heating difference (Fig. 15). Changes in the hydrological cycle and the atmosphere produced the heating and vertical motion changes. A positive feedback on the water budget enhanced these changes. Figure 16 shows the D2 minus G2 difference in the vertical motion averaged from  $100^\circ$  to  $115^\circ\text{E}$ . Relative subsidence dom-

inated almost the entire atmosphere over the test area except near the surface above the center of the desertification area. Meanwhile, rising motion was enhanced (or descending motion was weakened) to the south of the test area, where there was a rainfall increase.

To more clearly see these interaction processes, JJA mean differences for a number of variables between ensemble D2 and G2 over three regions are listed in

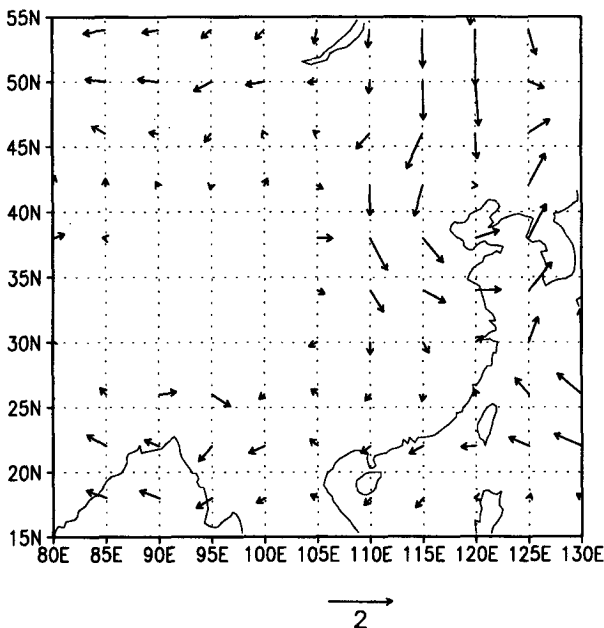


FIG. 13. JJA wind vector difference at 700 mb for ensemble D2 minus ensemble G2.

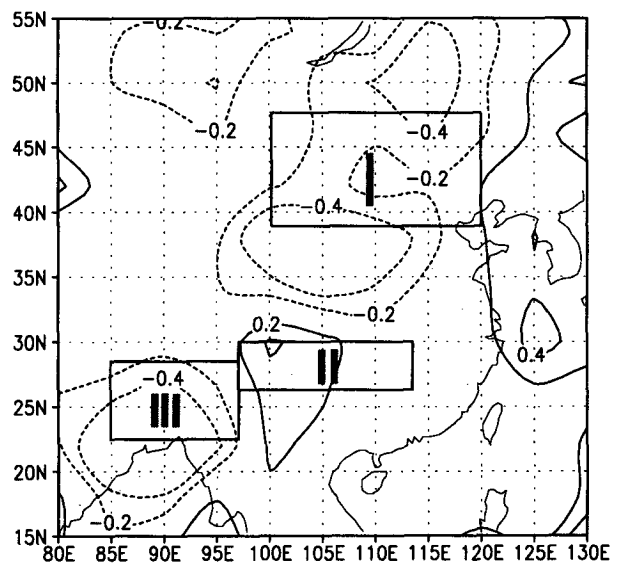


FIG. 15. JJA mean difference in total heating rate at 500 mb for ensemble D2 minus ensemble G2. Isolines are  $\pm 0.2, 0.4$  K/day. Dashed isolines are negative.

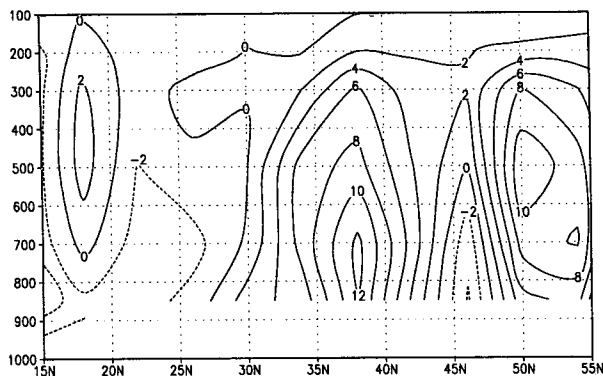


FIG. 16. JJA mean difference in zonally averaged vertical velocity from 100° to 115°E for ensemble D2 minus ensemble G2. Isotachs are  $\pm 5, 10, 15, 10^{-5} \text{ mb s}^{-1}$ . Dashed isotachs are negative.

Table 6 (see Fig. 15 for their locations). Region 1 is located in the reference area for D2 as discussed earlier. Region 2 is over the area with positive rainfall anomaly, and region 3 is close to the Bay of Bengal, which is the main moisture source for the East Asian continent. The three-month mean rainfall anomalies are consistent with the evaporation change in region 1 but are consistent with the changes in the vertically integrated moisture flux convergence in the other two regions. This confirms that different physical mechanisms are important over these regions. Although the rainfall change in region 3 is larger than that in region 1, relative to the mean it is only 10% change, smaller than the 18% reduction over Region 1. The major changes in regions 2 and 3 occurred during the last two months. The delayed responses indicate that the changes in these two regions were caused by the large-scale circulation changes induced by the desertification in region 1. The changes in vertical velocity and total diabatic heating are consistent with the rainfall changes in all three regions. The relative smaller change in averaged vertical velocity in region 1 was due to a rising motion area caused by the hot surface (Fig. 16).

5. Discussion and summary

This is a sensitivity study to test the impact of and mechanisms for desertification in the Mongolian and Inner Mongolian grassland on the regional climate.

Most of China has experienced a drying trend coincident with the land surface degradation in the Inner Mongolian grassland since the 1950s. Because the drought is not as severe as that in the Sahel, it has not been the subject of intensive GCM studies. In particular, the relationship between land surface degradation and drought has not been tested in GCM numerical experiments.

The numerical experiments presented in this study show that desertification in the Mongolian and the Inner Mongolian grassland has an impact on the regional climate and, in particular, on some important features of the East Asian summer monsoon. I have presented the results from ensemble means, but the impact was similar in individual cases. This impact was not limited to the desertification area and extended to the south of the desertification area. The reduction in evaporation mainly occurred within the desertification area, accompanied by reduced rainfall and increased surface temperature. The reduction in atmospheric diabatic heating was mainly due to reduced convective heating above the surface layer accompanied by enhanced relative descending motion over the desertification area and the adjacent area to the south. The monsoon flow was weakened in the desertification experiments.

Summer Asian monsoon variability is highly correlated with variability of the subtropical high (Zhu et al. 1979). In this study, the model results did not show substantial variations of the subtropical high in response to land surface changes. More experiments are needed to investigate the impact of the land surface degradation on the subtropical high and on other features related the East Asian monsoon.

We have conducted several numerical experiments to investigate the impact of the land surface degradation on the climate for different regions, for example, a Sahel drought study (Xue and Shukla 1993) and a U.S. prediction study (Xue et al. 1996b). All of these experiments showed the reduced rainfall and increased surface temperature over areas with land surface degradation. However, the responses over adjacent areas were quite different. In both the Sahel and Mongolian and Inner Mongolian grassland numerical experiments, the model simulated a positive rainfall anomaly to the south of the test area, which has not been found in the U.S. prediction study. The positive rainfall anomalies in the Sahel study and this study also had different fea-

TABLE 6. Simulated JJA differences for three regions. VMFC is the vertical integrated moisture flux convergence. TDBH is the total diabatic heating rate. Both vertical velocity and TDBH in the table area at the 500-mb level.

Region	Rainfall (mm/mo)	VMFC (mm/mo)	Evaporation	Vertical velocity ( $10^{-5} \text{ mb s}^{-1}$ )	TDBH (K/day)
1	-16.7	2.5	-21.1	4.7	-0.3
2	11.1	11.2	0	-5.7	0.2
3	-34.3	-37.5	0	8.5	-0.4

tures. Compared with the Sahel desertification experiment, the area associated with the positive rainfall anomaly in China was displaced farther south of the desertification area. This difference in response may be related to a number of factors, such as the local atmospheric circulation, orography, or the extent and degree of land surface degradation; this should be investigated further.

Despite that the desertification area in ensemble D1 is 40% larger than in D2, the flux differences between ensembles D1 and G1, and D2 and G2, were very similar. The magnitude of some energy component anomalies in ensemble D2 is larger than in ensemble D1 (Table 4). The simulated rainfall anomaly amounts are also very similar (Table 5). The differences between the two desertification maps (D1, D2) were mainly in the western part of the desertification area between 95° and 102°E. An increase in the desertification area over this region did not have a large impact on the results.

In an African drought study, Charney (1975) demonstrated that radiative cooling could generate sinking motion, which might cause reduced rainfall in tropical Africa. There was no moisture in his simple model. Using a coupled biosphere-atmosphere model with a complete hydrological cycle, this study reveals that although the longwave radiation loss at the top of the atmosphere increased in the desertification experiments (as discussed in section 4), the dominant component of the reduction in the diabatic heating is the reduction in convective heating.

**Acknowledgments.** This study was motivated by the IMGRASS (Inner Mongolia Grassland-Atmosphere Surface Study) program. The author would like to thank Drs. J. Shukla, T. C. Yeh (D. Z. Ye), and Xiuji Zhou and Professors Hai Lin and K.-N. Liou for supporting this study. I would also like to thank Professors Longxuan Chen, Mike Hulme, Youling Liang, Daren Lu, and Zhenda Zhu and the Oak Ridge National Laboratory for providing observational data and information for this study. Special thanks for Dr. Guoxiong Wu's support and very helpful discussions. The author would like to thank Mike Fennessy for helping with the numerical experiments and for suggestions on the manuscript, and also Fanrong J. Zeng for graphical assistance. This work was conducted under support from the National Science Foundation (NSF) and the National Aeronautics and Space Administration (NASA) through NSF Grants EAR-94-05431, ATM-93-41271, and ATM-93-21354, and the National Oceanic and Atmospheric Administration through NOAA Grant NA46GP0340-02. Computational support was provided by the NCAR Scientific Computing Division and NASA Center for Computational Sciences.

#### REFERENCES

- Alpert, J. C., M. Kanamitsu, P. M. Caplan, J. G. Sela, G. H. White, and E. Kalnay, 1988: Mountain induced gravity wave drag parameterization in the NMC medium-range forecast model. *Proc. Eighth Conf. on Numerical Weather Prediction*, Baltimore, MD, Amer. Meteor. Soc., 726-733.
- Anthes, R. A., 1977: A cumulus parameterization scheme utilizing a one-dimensional cloud model. *Mon. Wea. Rev.*, **105**, 270-300.
- Charney, J. G., 1975: Dynamics of deserts and drought in the Sahel. *Quart. J. Roy. Meteor. Soc.*, **101**, 193-202.
- Chen, L., Q.-G. Zhu, H.-B. Luo, J. He, M. Tong, and Z. Feng, 1991: *The East Asian Monsoon* (in Chinese). 1st ed. Meteorological Press, 362 pp.
- , M. Dong, and Y. Shao, 1992: The characteristics of interannual variations of the East Asian monsoon. *J. Meteor. Soc. Japan*, **70**, 397-421.
- , Y. Shao, and Z. Ren, 1994: Climate change in China during the past 70 years and its relationship to the variation of monsoon. *Climate-Biosphere Interaction*, R. G. Zepp, Ed., Wiley and Sons, 31-50.
- Davies, R., 1982: Documentation of the solar radiation parameterization in the GLAS Climate Model. NASA Tech. Memo 83961, NASA/Goddard Space Flight Center, 57 pp.
- DCIAP, 1991: Chinese 336-station 10-day temperature data in data category. Data Center at the Institute of Atmospheric Physics, Beijing, People's Republic of China.
- Dickinson, R. E., and A. Henderson-Sellers, 1988: Modeling tropical deforestation: A study of GCM land-surface parameterizations. *Quart. J. Roy. Meteor. Soc.*, **114**, 439-462.
- Dong, G., 1989: The desertification problem in China. *Climate Blue Book in China* (in Chinese), Science and Technology Information Press, 286-290.
- Dorman, J. L., and P. Sellers, 1989: A global climatology of albedo, roughness length and stomatal resistance for atmospheric general circulation models as represented by the Simple Biosphere Model (SiB). *J. Appl. Meteor.*, **28**, 833-855.
- Dregne, H. E., and N. T. Chou, 1992: Global desertification dimensions and costs. *Degradation and Restoration of Arid Lands*, Texas Tech. University, 249-282.
- Fennessy, M. J., J. L. Kinter III, B. Kirtman, L. Marx, S. Nigam, E. Schneider, J. Shukla, D. Straus, A. Vernekar, Y. Xue, and J. Zhou, 1994: The simulated Indian monsoon: A GCM sensitivity study. *J. Climate*, **7**, 33-43.
- Fu, C. B., 1992: Transitional climate zones and biome boundaries: A case study from China. *Landscape Boundaries, Consequences for Biotic Diversity and Ecological Flows*, A. J. Hansen and F. D. Castri, Eds., Springer-Verlag, 394-402.
- Harshvardhan, R. Davies, D. A. Randall, and T. G. Corsetti, 1987: A fast radiation parameterization for general circulation models. *J. Geophys. Res.*, **92**, 1009-1016.
- Hou, Y.-T., 1990: Cloud-radiation-dynamics interaction. Ph.D. dissertation, University of Maryland, 209 pp. [Available from the University of Maryland, College Park, College Park, MD 20742.]
- Hulme, M., 1992: A 1951-80 global land precipitation climatology for the evaluation of general circulation models. *Climate Dyn.*, **7**, 57-72.
- Kinter, J. L., III, J. Shukla, L. Marx, and E. K. Schneider, 1988: A simulation of the winter and summer circulations with the NMC global spectral model. *J. Atmos. Sci.*, **45**, 2486-2522.
- Kuchler, A. W., 1983: World map of natural vegetation. *Goode's World Atlas*, 16th ed., Rand McNally, 16-17.
- Kuo, H. L., 1965: On formation and intensification of tropical cyclones through latent heat release by cumulus convection. *J. Atmos. Sci.*, **22**, 40-63.
- Lacis, A. A., and J. E. Hansen, 1974: A parameterization for the absorption of solar radiation in the earth's atmosphere. *J. Atmos. Sci.*, **31**, 118-133.
- Lamb, P. J., 1978: Large-scale tropical Atlantic surface circulation patterns associated with sub-Saharan weather anomalies. *Tellus*, **30**, 240-251.
- Liang, Y. L., L. Song, and X. Wang, 1992: Variations of drought and flood during summer monsoon active seasons in China and its

- impact. *Studies of the Long Term Weather Forecast and the Sun-Earth Relationship* (in Chinese), J.-J. Zhang and R.-H. Huang, Eds., Ocean Press, 165–173.
- Mathews, E., 1984: Prescription of land-surface boundary conditions in GISS GCM II: A simple method based on high-resolution vegetation data bases. NASA Tech. Memo. 86096, 20 pp. [NTIS N8524508.]
- , 1985: Atlas of archived vegetation, land-use and seasonal albedo data sets. NASA Tech. Memo. 86199, 53 pp. [NTIS N8431761.]
- Meehl, G., 1987: The annual cycle and interannual variability in the tropical Pacific and Indian Ocean region. *Mon. Wea. Rev.*, **115**, 27–50.
- Mellor, G. L., and T. Yamada, 1982: Development of a turbulence closure model for geophysical fluid problems. *Rev. Geophys. Space Phys.*, **20**, 851–875.
- Nobre, C. A., P. J. Sellers, and J. Shukla, 1991: Amazonian deforestation and regional climate change. *J. Climate*, **4**, 957–988.
- Sela, J. G., 1980: Spectral modeling at the National Meteorological Center. *Mon. Wea. Rev.*, **108**, 1279–1292.
- Sellers, P. J., Y. Mintz, Y. C. Sud, and A. Dalcher, 1986: A simple biosphere model (SiB) for use within general circulation models. *J. Atmos. Sci.*, **43**, 505–531.
- Shen, S., and K. M. Lau, 1995: East Asian summer monsoon and tropical sea surface temperature. *J. Meteor. Soc. Japan*, **73**, 105–124.
- Slingo, J. M., 1987: The development and verification of a cloud prediction scheme for the ECMWF model. *Quart. J. Roy. Meteor. Soc.*, **103**, 29–43.
- Tiedtke, M., 1984: The effect of penetrative cumulus convection on the large-scale flow in a general circulation model. *Beitr. Phys. Atmos.*, **57**, 216–239.
- Vose, R. S., R. Keim, R. L. Schmoyer, T. R. Karl, P. M. Steuer, J. K. Eischeid, and T. C. Peterson, 1992: The global historical climatology network: Long-term monthly temperature, precipitation, sea level pressure, and station pressure data. CDIAC-53, NDP-041, Oak Ridge National Laboratory, Oak Ridge, TN, 189 pp.
- Willmott, C. J., and K. Klink, 1986: A representation of the terrestrial biosphere for use in global climate studies. ISLSCP *Proc. Int. Conf.*, Rome, Italy, European Space Agency, 109–112.
- Xue, Y., 1995: The impact of desertification in the Mongolian and the Inner Mongolian grassland on the East Asian monsoon. COLA Tech. Rep. 11, 50 pp. [Available from COLA, Calverton, MD 20705.]
- , and J. Shukla, 1993: The influence of land surface properties on Sahel climate. Part I: Desertification. *J. Climate*, **6**, 2232–2245.
- , and ———, 1994: The influence of land surface properties on Sahel climate. Part II: Afforestation. *J. Climate*, in press.
- , K.-N. Liou, and A. Kasahara, 1990: Investigation of the biophysical feedback on the African climate using a two-dimensional model. *J. Climate*, **3**, 337–352.
- , P. J. Sellers, J. L. Kinter III, and J. Shukla, 1991: A simplified biosphere model for global climate studies. *J. Climate*, **4**, 345–364.
- , N. Bastable, P. Dirmeyer, and P. Sellers, 1996a: Sensitivity of simulated Amazonian climate to changes in land surface parameterization—A study using ABRACOS data. *J. Appl. Meteor.*, **35**, 386–400.
- , M. J. Fennessy, and P. J. Sellers, 1996b: Impact of vegetation properties on U.S. weather prediction. *J. Geophys. Res.*, **101**(D3), 7419–7430.
- , F. J. Zeng, and C. A. Schlosser, 1996c: SSiB and its sensitivity to soil properties—A case study using HAPEX-Mobilhy data. *Global Planet. Change*, **13**, 183–194.
- Yan, Z. W., J.-J. Ji, and D. Z. Ye, 1990: Northern hemispheric summer climate jump in the 1960s (I). *Sciences in China*, **B33**, 1092–1101.
- Yanai, M., and C. Li, 1994: Interannual variability of the Asian summer monsoon and its relationship with ENSO, Eurasian snow cover and heating. *Proc. Int. Conf. on Monsoon Variability and Prediction*, Trieste, Italy, World Meteorological Organization, WMO/TD No. 619, Vol. I, 27–34.
- Yang, Z.-L., R. E. Dickinson, A. Henderson-Sellers, and A. J. Pitman, 1995: Preliminary study of spin-up processes in land surface models with the first stage data of project for intercomparison of land surface parameterization schemes phase 1(a). *J. Geophys. Res.*, **100**, 16 553–16 578.
- Ye, D.-Z., 1992: *The Preliminary Study of the Global Change in China, Part 1* (in Chinese). 1st ed. Meteorological Press, 101 pp.
- , and P. Q. Chen, 1992: *The Preliminary Study of the Global Change in China, Part 2* (in Chinese). 1st ed. Meteorological Press, 279 pp.
- Zhu, Q.-G., J. Lin, and S. Shou, 1979: *Synoptic Meteorology: Principle and Method* (in Chinese). 1st ed. Meteorology Press, 535 pp.
- Zhu, Z., and W. Tao, 1993: Trends of desertification and its rehabilitation in China. *Desertification Bulletin*, **22**, 27–30.
- , S. Liu, and X. Di, 1988: *Desertification and Rehabilitation in China*. 1st ed. Academic Press, 126 pp.